*Clays and Clay Minerals*, Vol. 64, No. 4, 472–487, 2016.

# ION ADSORPTION AT CLAY-MINERAL SURFACES: THE HOFMEISTER SERIES FOR HYDRATED SMECTITE MINERALS

THOMAS UNDERWOOD*, VALENTINA ERASTOVA, AND H. CHRIS GREENWELL*
Department of Earth Sciences, Durham University, Science Labs, Durham DH1 3LE, UK

**Abstract**—Many important properties of clay minerals are defined by the species of charge-balancing cation. Phenomena such as clay swelling and cation exchange depend on the cation species present, and understanding how the cations bind with the mineral surface at a fundamental level is important. In the present study the binding affinities of several different charge-balancing cations with the basal surface of the smectite mineral, montmorillonite, have been calculated using molecular dynamics in conjunction with the well-tempered metadynamics algorithm. The results follow a Hofmeister series of preferred ion adsorption to the smectite basal surfaces of the form:

$$K^+ > Na^+ > Ca^{2+} > Cs^+ > Ba^{2+}$$

The results also revealed the energetically favorable position of the ions above the clay basal surfaces. Key features of the free-energy profiles are illustrated by Boltzmann population inversions and analyses of the water structures surrounding the ion and clay surface. The results show that weakly hydrated cations ($K^+$ and $Cs^+$) preferentially form inner-sphere surface complexes (ISSC) above the ditrigonal siloxane cavities of the clay, while the more strongly hydrated cations ($Na^+$) are able to form ISSCs above the basal O atoms of the clay surface. The strongly hydrated cations ($Na^+$, $Ca^{2+}$, and $Ba^{2+}$), however, preferentially form outer-sphere surface complexes. The results provide insight into the adsorption mechanisms of several ionic species on montmorillonite and are relevant to many phenomena thought to be affected by cation exchange, such as nuclear waste disposal, herbicide/pesticide–soil interactions, and enhanced oil recovery.

**Key Words**—Binding Affinity, Cation Exchange, Molecular Dynamics, Montmorillonite, Well-tempered Metadynamics.

## INTRODUCTION

Clays are naturally occurring layered phyllosilicate minerals which are known to play an important role in many geochemical processes, whether within marine systems, terrestrial soils, or the subsurface in aquifers and oil reservoirs (Bergaya *et al.*, 2006). Because of their large surface area, permanent negative charge, and cation exchange properties, smectites have found an increasing multitude of practical applications and have been studied extensively using analytical laboratory-based techniques. In recent years, computational techniques, such as molecular dynamics (MD) and *ab initio* calculations (including density functional theory – DFT), have become increasingly beneficial in helping to improve understanding of clay-mineral properties at the atomistic level (Greenwell, 2006; Suter, 2009).

Three types of clay mineral surfaces are apparent: (1) the external basal surfaces; (2) the external clay edges; and (3) the interlayer basal surfaces. The adsorption and exchange of cations at the different clay-mineral surfaces can alter the physical and chemical properties of the clay mineral comprehensively. Interlayer bound K, for example, acts as a swelling inhibitor, preventing hydration and expansion of the interlayer region, while Na promotes swelling when present in smectite-like clay minerals (Boek *et al.*, 1995). Because of their use as a barrier material in underground nuclear-waste repositories, understanding how radioactive cations, such as Ba and Cs, adsorb to clay-mineral surfaces, with potentially significant ramifications for nuclear-waste repository design and operation, has become increasingly important (Ngouana *et al.*, 2014). Because the behavior of clay minerals depends on the species of charge-balancing cation, understanding how the cation binds with the mineral surface and how the cation's affinity to the surface differs from ion to ion is important; however, studying the behavior of cations at clay-mineral surfaces and within interlayers is particularly challenging. Nuclear magnetic resonance (NMR) studies have been undertaken on non-paramagnetic synthetic clays offering insight into ion dynamics and distribution (Bowers *et al.*, 2008), while the use of quasi-elastic neutron scattering (QENS) on well-ordered vermiculite clay gels, as well as smectites, has allowed

* E-mail address of corresponding author:
chris.greenwell@durham.ac.uk
thomas.underwood@durham.ac.uk
DOI: 10.1346/CCMN.2016.0640310

This paper is published as part of a special issue on the subject of 'Computational Molecular Modeling.' Some of the papers were presented during the 2015 Clay Minerals Society-Euroclay Conference held in Edinburgh, UK.

the study of cation/water structure in interlayers (Swenson *et al.*, 2000; Marry *et al.*, 2013). Additional insight into swelling energetics and structure has been obtained from computer simulation of hydrated clay minerals ((Boek *et al.*, 1995; Shroll and Smith, 1999; Boek and Sprik, 2003).

A key property of many clay minerals is cation exchange, where a more labile cation is substituted by a less labile one to modify the clay-mineral activity. The traditional view of alkaline metal-ion selectivity for cation exchange follows a Hofmeister-like series (Hanshaw, 1964):

$$K^+ \approx Cs^{2+} > Na^+ > Ba^{2+} > Ca^{2+}$$

The reasoning for this sequence has been postulated through (at least) two arguments: (1) the ratio of hydrated cation size to interlayer spacing (Gast, 1969, 1972), whether the hydrated ion can fit within the steric cavities of the interlayer spacing; and (2) the cations' ability to partially dehydrate at the mineral surface and thus form strong inner-sphere surface complexes (Eisenman, 1962).

While many historical studies of the Hofmeister series have examined the hydration properties of the ions, ion–macromolecule interactions clearly also play a dominant role (Zhang and Cremer, 2006).

Previous computational work has been able to elucidate some of the properties of cation-exchange clay systems. While the binding energy between K and montmorillonite is greater than that between Cs and montmorillonite, the Cs–montmorillonite system is more stable overall due to the decreased enthalpy of hydration of the K over the Cs in the solvent phase (Teppen and Miller, 2006). The result shows how important it is to consider not only the effect of the ion interacting with the mineral surface, but also with the bulk solvent phase. Previously, this has been achieved using an explicit solvent bath (Rotenberg *et al.*, 2007) or through the use of thermodynamic cycles (Rotenberg *et al.*, 2009).

In the present study, classical MD simulations were used in conjunction with well-tempered metadynamics to determine the free energy of adsorption of, as well as the competition between, cations at the hydrated basal surfaces of montmorillonite. The following simulations are particularly pertinent to understand the phenomenon of multicomponent cation exchange during low-salinity enhanced oil recovery, whereby organic matter, bridged to the surface through divalent cations, becomes desorbed from the basal surface of a clay mineral (Underwood *et al.*, 2015).

## METHODS

### *Model setup*

The clay unit cell used in this study was a Wyoming-like montmorillonite with atomic coordinates taken from the *American Mineralogist Crystal Structure Database* (Downs and Hall-Wallace, 2003; Viani *et al.*, 2002) and with stoichiometry:

$$M^+[Al_3Mg_1][Si_8O_{20}](OH)_4.nH_2O$$

In this model, the octahedral sheets of the clay contained one Mg atom for every three Al atoms, and no isomorphic substitutions occurred in either tetrahedral sheet. The resulting unit cell possessed a single net negative charge, corresponding to a surface charge density of ~0.35 C $m^{-2}$. Periodically replicated supercells were generated containing one layer of montmorillonite, consisting of 18 unit cells ($6 \times 3 \times 1$) with dimensions of ~30 Å × 30 Å × 100 Å, and a pore spacing of ~90 Å (Figure 1). Montmorillonite structures initially occupied the region $0 < z < 7$ Å in all of the following simulations, and the clay position varied little over the

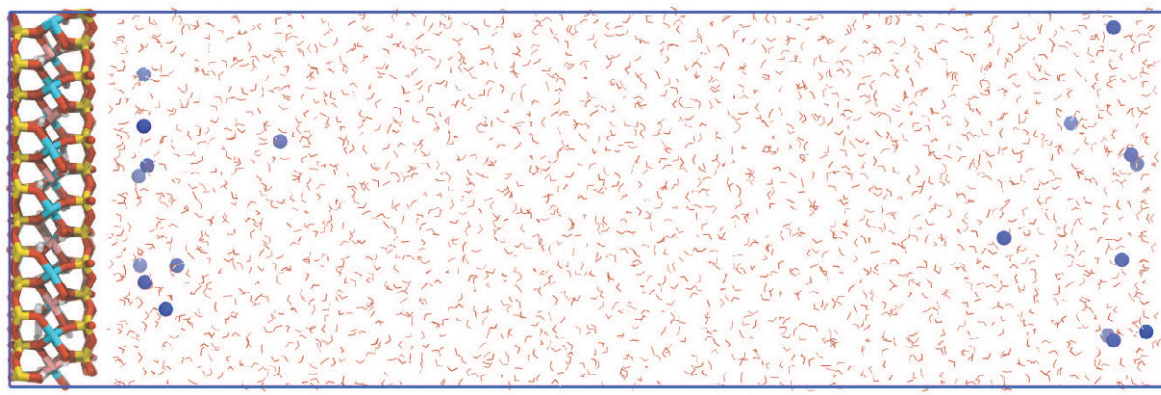

Figure 1. An example supercell, used in the simulations, with $Na^+$ cations (dark blue) interacting with montmorillonite. The color scheme of the clay is as follows: Si – yellow; O – red; Al – blue; Mg – pink, and H – white. Also presented in stick form are the water molecules within the nano-pore spacing. Periodic boundaries were used in all directions, and the simulation supercell has dimensions of ~30 Å × 30 Å × 100 Å (note that the figure is flipped here, such that the *z* direction is across the figure, from left to right).

https://doi.org/10.1346/CCMN.2016.0640310 Published online by Cambridge University Press

timescales modeled. The simulation super-cells were subsequently hydrated (with ~2500 water molecules) and the requisite number of cations added to the system to charge balance the montmorillonite surface. In total, five independent systems were set up, differing according to the type of charge-balancing cation. The cations considered in the present study were $Na^+$, $K^+$, $Cs^+$, $Ca^{2+}$, and $Ba^{2+}$.

The clay mineral has been modeled using the *ClayFF* force field (Cygan *et al.*, 2004), which is specifically parameterized to model layered minerals and designed such that all the interactions within, and the entire structure of, the clay is described wholly by the non-bonded Lennard-Jones and Coulomb potentials (hydroxyl groups are bonded as an exception). The standard *SPC* water model (Berendsen *et al.*, 1987) has been used to parameterize the solvent. Ion parameters were taken from a variety of sources and are consistent with the *ClayFF* and *SPC* force fields (Aaqvist, 1990; Smith and Dang, 1994a, 1994b; Koneshan *et al.*, 1998; Cygan *et al.*, 2004).

### *Equilibration details*

All simulations were initialized with an energy minimization run to reduce any excessive force on any one atom. This was accomplished using a steepest-descents algorithm, with convergence achieved once the maximum force on any one atom was <10 kJ $mol^{-1}$ $Å^{-1}$. Subsequently, equilibration simulations were run for a 10 ns period in the constant number of particles, pressure, and temperature (NPT) ensemble at 300 K and 1 bar using a velocity-rescale Berendsen thermostat, temperature coupling constant set to 0.1 ps, and a semi-isotropic Berendsen barostat, with pressure-coupling constant of 1 ps. The Berensden thermostat and barostat offered swift equilibration of the system, and convergence was adjudged to have been attained once both the $z$ spacing and potential energy had converged.

### *Metadynamic details*

After equilibration, the super-cell was translated along the $z$ axis such that the apical O atoms of the silicate sheet of the lowest clay basal surface lay upon the $z$ = 0 Å plane. Before any free-energy calculations were carried out, the clay model was fixed in place as a rigid structure. Then, a single cation was chosen, at random, to be the test ion on which the free-energy calculations were performed. All other ions in the system were free to move according to the force fields used in the simulations.

The well-tempered metadynamics algorithm was used to explore the free-energy curve of the clay–ion–water system as a function of the clay−ion separation (*i.e.* the reaction coordinate). During the metadynamics simulation, the forces calculated with conventional MD are modulated by adding Gaussian functions to the Hamiltonian at points along the reaction coordinate (Barducci *et al.*, 2008). Here, 25 separate, well-tempered metadynamic simulations were run, five for each cation type. Running multiple ensemble simulations when calculating equilibrium thermodynamic properties, such as binding energies, is important because any one simulation is unlikely to sample sufficiently all of the phase-space required to satisfy the ergodic hypothesis (Coveney and Wan, 2016). Five separate ensemble simulations were deemed sufficient to reduce the total uncertainty in the free-energy profiles generated using the metadynamic algorithm in the present work. Each metadynamic simulation was run for 200 ns at 300 K in the constant number of particles, volume, and temperature (NVT) ensemble. Gaussian functions with an initial height of 1.20 kJ/mol, a width of 0.10 Å, and a bias factor of 10 were applied to the Hamiltonian every 0.5 ps. Convergence of the well-tempered metadynamics algorithm was ensured by observing that the Gaussian height tended to zero throughout all well-tempered metadynamic simulations. Checks were also made to ensure that the test ion sampled all of the available planar $xy$ space, in conjunction with clay−ion separation space.

Due to the translational symmetry of the clay mineral, additional bias potentials were added to the test ion. This constrained the ion within a single unit cell of the montmorillonite surface. Any additional sampling would simply increase computational time, yet yield no additional information. This constraint was achieved using a spring-like bias of the form:

$$V_{wall}(x) = k(x - x_{max})_4 \in x > x_{max} \quad (1)$$

where k is the elastic spring constant of the wall, set to 500 kJ/mol, and $x_{max}$ is the lower limit of the wall. Similar boundaries were established to constrain the lower bounds of the test ion in the $x$ direction, to constrain the ion in the $y$ direction, as well as to keep the test ion within 10 Å of the mineral surface.

### *Simulation details*

All MD simulations were performed using *GROMACS* version 4.6.7 (Pronk *et al.*, 2013) with the Particle-Mesh-Ewald summation method for determining the electrostatic contribution, with a real-space electrostatic cut-off of 12 Å, a reciprocal space precision of $10^{-5}$, in addition to a van der Waals cut-off distance of 12 Å. The well-tempered metadynamic algorithm was implemented using *PLUMED* 2.1.2 (Bonomi *et al.*, 2009; Tribello *et al.*, 2014), which works in conjunction with *GROMACS*, while all images of the simulated structures have been produced using *VMD* 1.9.2 (Humphrey, 1996).

### *Analysis details*

All free-energy analyses were carried out using the internal tools for *GROMACS* 4.6.7 and *PLUMED* 2.1.2 (Bonomi *et al.*, 2009; Tribello *et al.*, 2014). The Python

https://doi.org/10.1346/CCMN.2016.0640310 Published online by Cambridge University Press

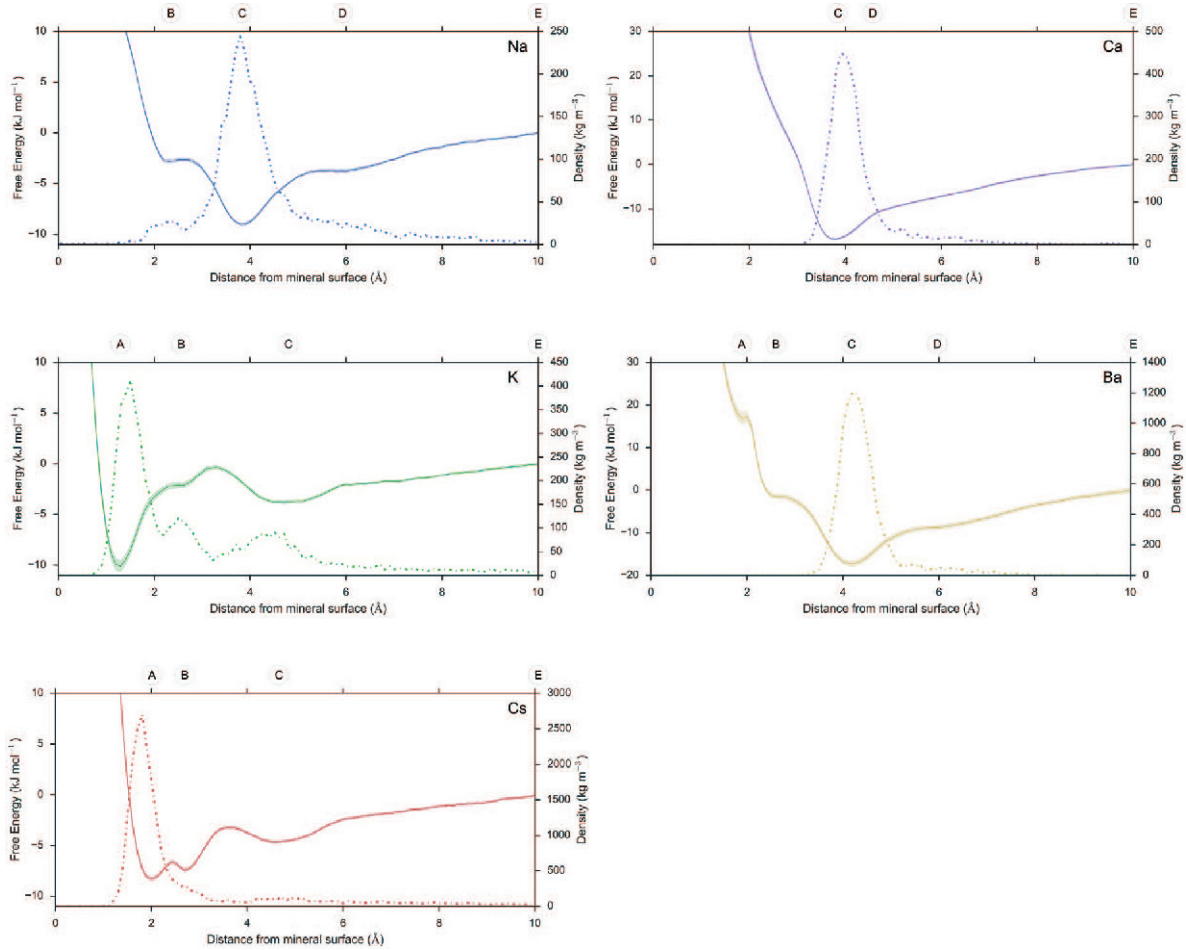


Figure 2. Free-energy profiles of all cations as a function of clay−ion separation. Note that the narrow shaded regions indicate the standard error in the metadynamic calculation at each point along each of the free-energy diagrams. Also presented is the ion density as a function of distance from the clay basal surface (dotted line). The points A, B, C, D, and E are noted as interesting features within the free-energy diagrams and are shown at the top of each of the parts of the figure.

module *MDAnalysis* 0.13 (Michaud-Agrawal *et al.*, 2011) and *Matplotlib* 1.5.1 (Hunter, 2007) were used to further analyse simulation trajectories and generate figures of water densities and radial distribution functions (RDFs). The plotted free-energy profiles (Figure 2) present the average free energy at each point along the reaction coordinate as a bold line and the relative error (plus-minus) is presented in the shaded area. The values of individual binding energies are given with the corresponding standard error as plus-minus. All ion-density profiles (dotted lines in the free-energy profiles) were calculated using the last 5 ns of the 10 ns equilibration period, *i.e.* from an unbiased simulation.

## RESULTS

Note, in the first instance, the general shape of the free-energy curves (Figure 2). After a short-range repulsion between the ion and the mineral surface, and beyond the (often several) minima, the free-energy profiles plateau. In the long clay−ion separation limit, this plateau can be decomposed as a combination of clay ($F^{\text{clay}}_{\text{self}}$), ion ($F^{\text{ion}}_{\text{self}}$), and solvent ($F^{\text{water}}_{\text{self}}$) self energies; clay−water ($F^{\text{clay}}_{\text{hydration}}$) and ion−water ($F^{\text{ion}}_{\text{hydration}}$) hydration energies; as well as long-range interaction terms ($F^{\text{clay-ion}}_{\text{electrostatic}}$). The binding free energy ($F$), can be expressed as:

$$\lim_{z\to\infty} F(z) = F^{\text{clay}}_{\text{self}} + F^{\text{ion}}_{\text{self}} + F^{\text{water}}_{\text{self}} + F^{\text{clay}}_{\text{hydration}} + \mathrm{F}^{\text{ion}}_{\text{hydration}} + F^{\text{clay-ion}}_{\text{electrostatic}}(z) \quad (2)$$

This means that the overall binding energy ($\Delta F_{\text{binding}}$) of the ion to the surface can be calculated as:

$$\Delta F_{\text{binding}} = F(z_{\text{min}}) - \lim_{z\to\infty} F(z) \quad (3)$$

where $z_{\text{min}}$ is the location of the global-energy minimum with respect to clay−ion separation.

Note that at sufficiently large $z$, the individual self-energies of the unbound system and hydration terms in

https://doi.org/10.1346/CCMN.2016.0640310 Published online by Cambridge University Press

equation 2 are independent of $z$ because the hydration shells of the ion and clay no longer overlap. Thus, at large $z$, when comparing binding energies between different ion species, one needs only to consider the difference between the long-range clay−ion electrostatic term. Because all simulations have been run at the same temperature (300 K) and ionic strengths, the long-range electrostatic term, which can be described through Poisson-Boltzmann theory, is postulated to be equal for all different ions at any arbitrary $z$. The free-energy profiles can, therefore, justifiably, be normalized, subject to the boundary condition that for large clay−ion separation:

$$\lim_{z\to\infty} F(z) = 0 \quad (4)$$

Following this argument, a direct comparison of the binding free-energies differences between dissimilar species of monovalent and divalent cations have been calculated (Table 1).

*Free-energy profiles*

The free-energy profiles for all of the systems considered (Figure 2) highlight several points of interest along the reaction coordinate. These are marked by the points A, B, C, D, and E across the top of each part of Figure 2. To be consistent, the points correspond to the coordination states of the ion. In brief, A corresponds to a primary inner-sphere surface complex (ISSC); B corresponds to a secondary ISSC; C corresponds to an outer-sphere surface complex (OSSC), and D corresponds to a secondary hydration shell surface complex (SHSSC). These terms are explained below. The point E corresponds to a clay−ion separation of 10 Å, the maximal distance of the reaction-coordinate in the metadynamic simulations.

*Na-montmorillonite*

The free-energy profile for the Na-montmorillonite system (Figure 2 − Na) shows that for small separation distances (<2 Å) the montmorillonite−ion interaction is entirely repulsive. This represents the close-range repulsion between clay and ion due to electron wave-function overlap. Beyond this, the ion experiences three individual clay−ion separations of (meta)stable equilibria. The global minimum, and thus the most energetically favorable montmorillonite−sodium separation, is at 3.8 Å, with a binding energy of −9.00±0.35 kJ/mol (Figure 2 − Na(C)). A secondary, metastable minimum is located nearer to the clay surface, at a clay−sodium distance of 2.3 Å, with a binding energy of −2.76±0.43 kJ/mol (Figure 2 − Na(B)). A third, metastable minimum is located further from the clay surface, at a separation value of 6 Å and with a binding energy of −3.68±0.37 kJ/mol (Figure 2 − Na(D)).

The global minimum corresponds to a system where the $Na^+$ cation is fully hydrated and the ion's solvation shell is associated with the mineral surface *via* hydrogen bonding. This association can be observed in the overlapping water structures of the first hydration shell of the ion with the first hydration layer of the clay (Figure 3 − Na(C)). The phenomenon is well known, and referred to as an outer-sphere solvation complex (OSSC). In contrast, the metastable minimum nearer the clay surface corresponds to an inner-sphere solvation complex (ISSC), whereby the cation is only partially hydrated, and is directly adsorbed on the mineral surface *via* electrostatic interactions (Figure 3 − Na(B)). The metastable minimum farthest away from the clay surface corresponds to where the second hydration shell of the $Na^+$ ion overlaps with the first hydration layer of the clay (Figure 3 − Na(D)). This situation has been observed for several cations and is denoted hereafter as a secondary hydration shell surface complex (SHSSC). Also presented is the water structure surrounding the ion and clay at a clay−ion separation of 10 Å (Figure 3 − Na(E)). Note that at such distance, the hydration layers of the clay and ion no longer overlap.

The radial distribution functions (RDFs) between the $Na^+$ ion and water/basal clay O further reiterate that the minima correspond to ISSC and OSSC. For the ISSC (Figure 4 − Na(B)), the basal clay O atoms are shared with water O atoms in the first coordination shell of the ion. In contrast, for the OSSC (Figure 4 − Na(C)), the basal clay O atoms are contained within the second coordination shell of the ion. For the SHSSC (Figure 4 − Na(D)), the clay basal O atoms contribute to the third coordination shell of the $Na^+$ ion. Also presented is the

Table 1. Binding energies (kJ/mol) and stable clay−ion separations (Å) of cations to montmorillonite basal surfaces. The global energy minimum for each ion is given in bold. The Primary ISSC is defined as the inner-sphere complex located above the hexagonal siloxane cavity of the clay, whilst the secondary ISSC is the complex above a basal surface O.

| Ion | VdW radii | Primary ISSC | | Secondary ISSC | | OSSC | | SHSSC | |
|---|---|---|---|---|---|---|---|---|---|
| | | Separation | Energy | Separation | Energy | Separation | Energy | Separation | Energy |
| $Na^+$ | 2.35 | | – | 2.3 | −2.76 (0.43) | **3.8** | **−9.00 (0.35)** | 6.0 | −3.68 (0.37) |
| $K^+$ | 3.33 | **1.3** | **−10.56 (1.29)** | 2.6 | −2.46 (0.70) | 4.7 | −3.83 (0.37) | | – |
| $Cs^+$ | 3.83 | **2.0** | **−8.34 (0.40)** | 2.7 | −7.51 (0.38) | 4.6 | −4.64 (0.26) | | – |
| $Ca^{2+}$ | 2.87 | | – | | – | **3.8** | **−16.76 (0.41)** | | – |
| $Ba^{2+}$ | 3.81 | 1.9 | +18.26 (3.55) | 2.6 | −0.54 (1.82) | **4.2** | **−16.66 (1.46)** | 5.8 | −8.38 (1.25) |

https://doi.org/10.1346/CCMN.2016.0640310 Published online by Cambridge University Press

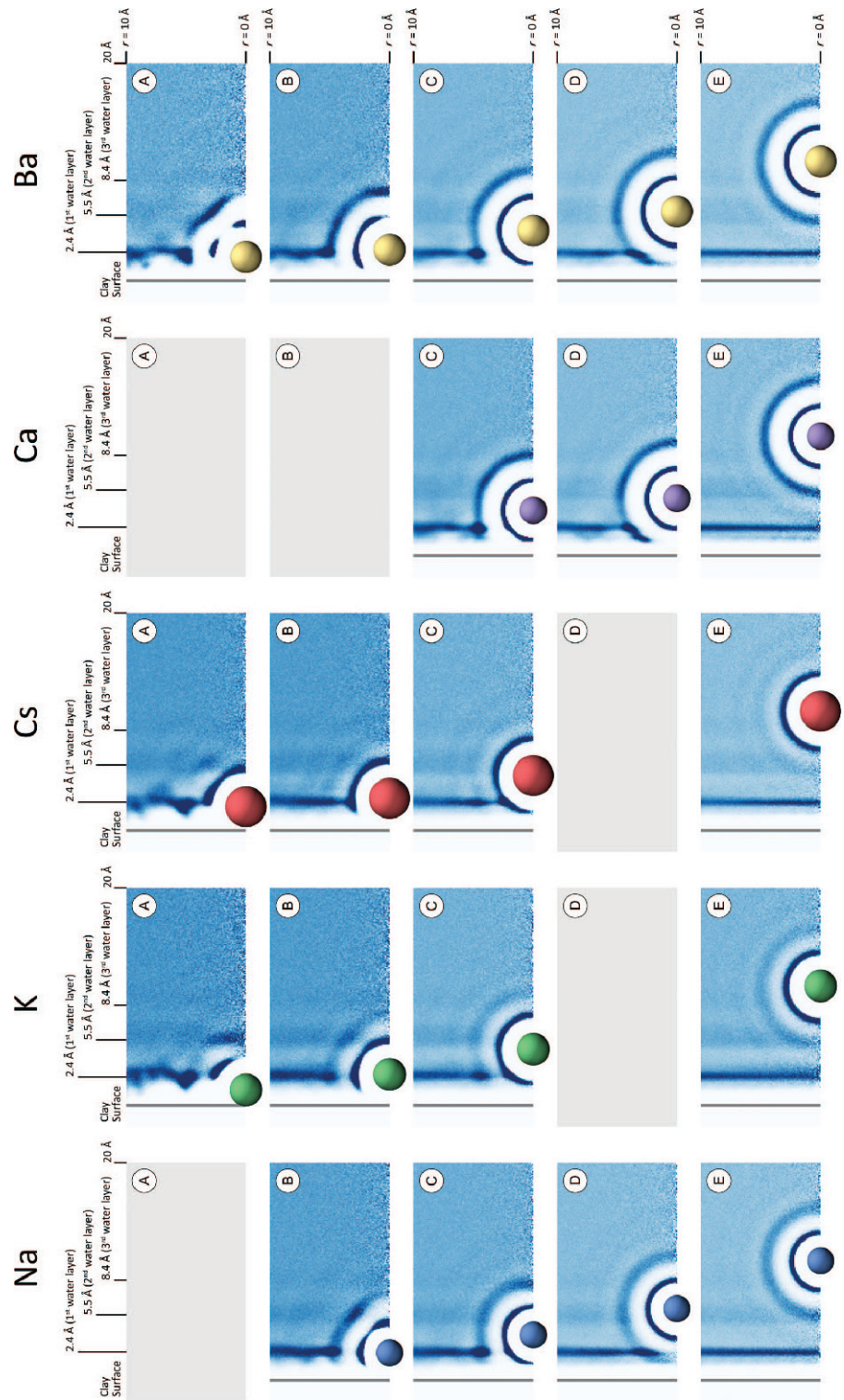


Figure 3. The water O density surrounding the clay and ion at the point of interest along the free-energy curve. The spheres represent the ion at the point of interest, whereby the radius of each ion corresponds to its van der Waals radius used in the simulations.

https://doi.org/10.1346/CCMN.2016.0640310 Published online by Cambridge University Press

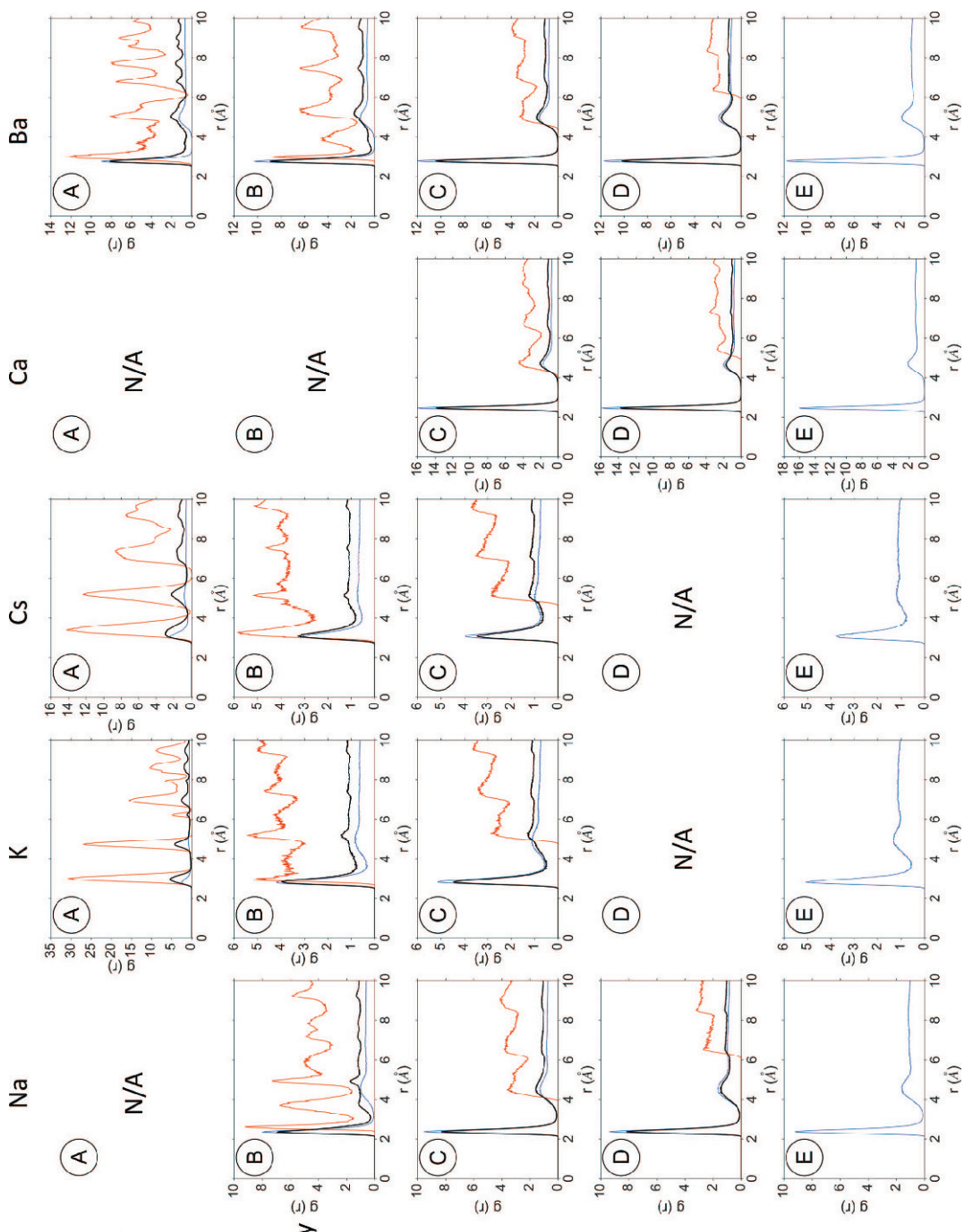


Figure 4. The RDFs between each cation and O atom at each point of interest along the free-energy diagram. Blue – RDF between cation and water O; orange – RDF between cation and clay O; and black –RDF between the cation and all O atoms.

https://doi.org/10.1346/CCMN.2016.0640310 Published online by Cambridge University Press

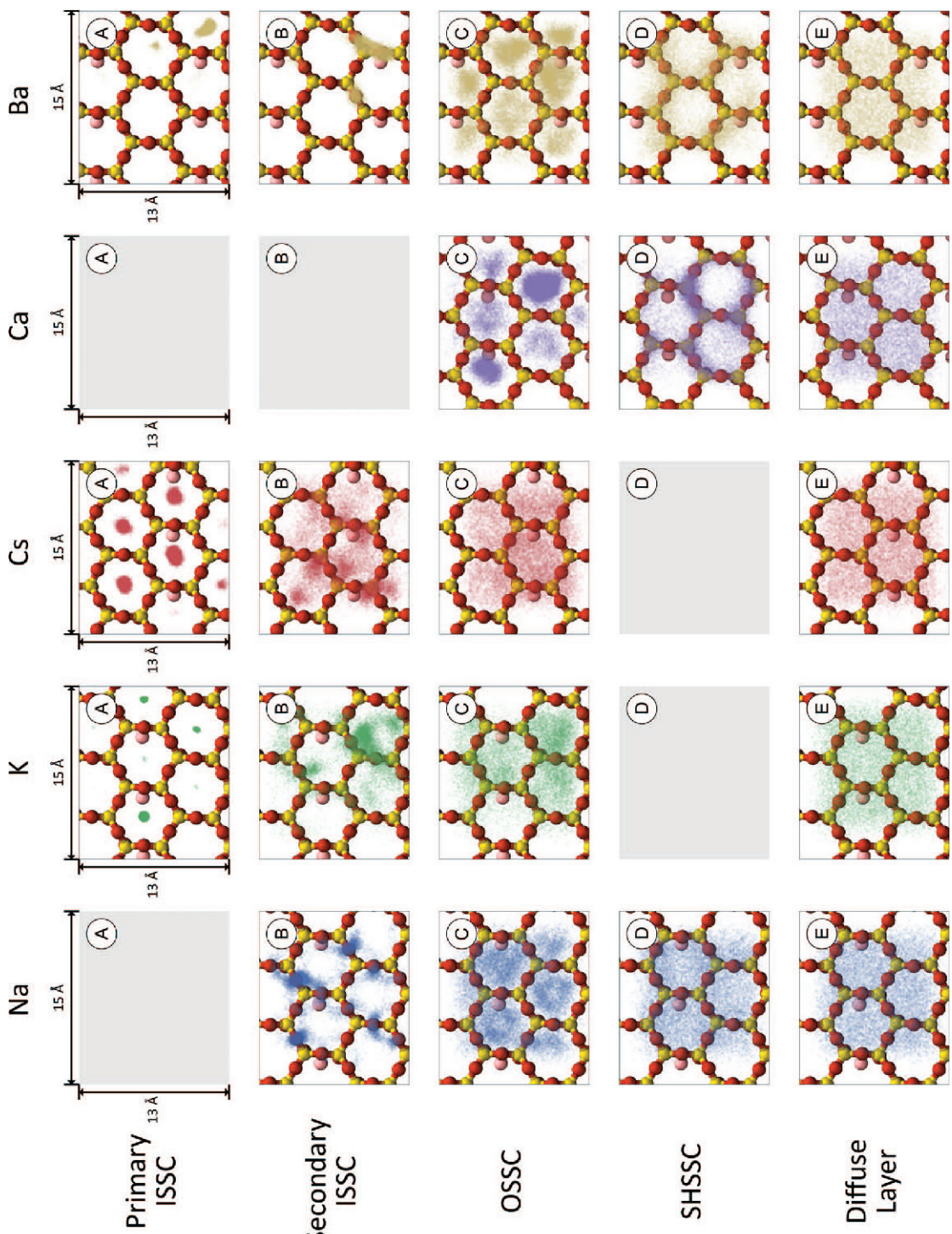


Figure 5. The *xy* planar density of the cations examined at each point of interest along the free-energy curve.

https://doi.org/10.1346/CCMN.2016.0640310 Published online by Cambridge University Press

RDF for the system at a clay–ion separation of 10 Å (Figure 4 – Na(E)). In this case the hydration layers of the ion and clay no longer interact and the resulting RDF is that of the $Na^+$ ion with bulk water.

The planar density of the ion above the mineral surface shows that, for the ISSC, the $Na^+$ ion is localized above a single basal clay O (Figure 5 – Na(B)). In contrast, the OSSC is less localized above the clay basal surface (Figure 5 – Na(C)), with a preference for location above one of the hexagonal siloxane cavities of the mineral surface. For the SHSSC and beyond, the ion's position above the basal clay surface is no longer localized, and is dispersed homogeneously across the unit cell (Figure 5 – Na(D) and Na(E)).

*K-montmorillonite*

The free-energy profile for K (Figure 2 – K) presents several features similar to that of Na. Again, beyond the typical close-distance repulsion, three separate (meta)-stable minima are observed. The global minimum, in this instance, is located near the surface of the mineral, at a montmorillonite–K separation of 1.3 Å, with a binding energy of −10.56±1.29 kJ/mol (Figure 2 – K(A)). The next most stable minimum is located at 4.7 Å, with a binding energy of −3.83±0.37 kJ/mol (Figure 2 – K(C)). A metastable minimum also exists between these two points at a clay–K separation of 2.6 Å with a binding energy of −2.46±0.70 kJ/mol (Figure 2 – Na(B)).

Focusing on the global energy minimum (point A), both the water structure (Figure 3 – K(A)) and the RDF (Figure 4 – K(A)) reveal that the ion forms an ISSC in its most energetically favorable state. In particular, the RDF shows that the first coordination shell of the $K^+$ ion is largely composed of clay O atoms. The *xy* planar density of the $K^+$ ion in its ISSC state (Figure 5 – K(A)) shows that the ion is extremely localized above the hexagonal cavities of the clay surface. This behavior is in contrast to the ISSC observed for Na. The terms primary ISSC and secondary ISSC are introduced here to denote the difference between these two different forms of ISSC. A primary ISSC denotes an ion that sits above one of the hexagonal cavities of the clay surface; the term secondary ISSC indicates that the ion sits above one of the basal O atoms of the clay.

The least energetically favorable metastable minimum is located at point B in the free-energy profile (Figure 2 – K(B)). The water structure (Figure 3 – K(B)) and RDF (Figure 4 – K(B)) indicate that this minimum is also an ISSC. The *xy* planar density of the ion above the surface (Figure 4 – K(B)) indicates that this is a secondary ISSC. The results show that K can stably form both primary, and secondary, inner-sphere surface complexes.

The most energetically favorable metastable minimum is located at point C in the free-energy profile (Figure 2 – K(C)). Here the $K^+$ ion forms an OSSC, as the first hydration shell of the ion overlaps with the first hydration layer of the clay (Figure 3 – K(C)). The RDF (Figure 4 – K(C)) also highlights that the basal clay O atoms coordinate within the second hydration shell of the K cation. Like the $Na^+$ ion, the OSSC of K is loosely localized above the hexagonal siloxane cavities of the basal surface, as evidenced by the *xy* planar density distribution (Figure 5 – K(C)). Beyond this point, the $K^+$ ion is not observed to form a SHSSC and moves freely across the *xy* plane (Figure 5 – K(E)).

*Cs-montmorillonite*

The free-energy diagram for the Cs-montmorillonite system (Figure 2 – Cs) is very similar to that of K. Again, three separate minima are observed. The global energy minimum is at a montmorillonite–Cs separation of 2.0 Å with a binding energy of −8.34±0.40 kJ/mol (Figure 2 – Cs(A)). The secondary minimum is at a clay–ion distance of 2.7 Å with a binding energy of −7.51±0.38 kJ/mol (Figure 2 – Cs(B)), and the tertiary minimum is located at a clay–ion distance of 4.6 Å with a binding energy of −4.64±0.26 kJ/mol (Figure 2 – Cs(C)).

The global minimum of Cs forms an ISSC as can be observed through the water structure (Figure 3 – Cs(A)) and Cs-O RDF results (Figure 4 – Cs(A)). Like K, the global energy minimum of Cs is localized above the hexagonal siloxane cavities of the clay surface (Figure 5 – Cs(A)) and is, therefore, observed to form primary ISSCs.

The second and third minima of Cs correspond to a secondary ISSC and OSSC, respectively, as shown by the overlapping of the water structures surrounding the ion and clay (Figure 3 – Cs (B) and Cs(C)), the overlapping O atoms in the RDFs (Figure 4 – Cs(B) and Cs(C)), as well as the ion localizations above the *xy* plane (Figure 5 – Cs(B) and Cs(C)). Much like K, therefore, Cs readily forms both secondary ISSCs and OSSCs. Unlike K, however, the secondary ISSC is more energetically stable than the OSSC.

*Ca-montmorillonite*

In contrast to the results for other ions presented so far, the free-energy profile for Ca showed only one stable minimum (Figure 2 – Ca). This minimum is at a clay–ion distance of 3.8 Å and has a binding energy of −16.76±0.41 kJ/mol (Figure 2 – Ca(C)). The water structures surrounding the Ca and clay in conjunction with the RDFs between ion and O atoms show that this global energy minimum is an OSSC. The water structure (Figure 3 – Ca(C)) shows that the first hydration shell of the Ca overlaps with the first hydration layer of the clay basal surface. Furthermore, the RDF (Figure 4 – Ca(C)) indicates that the basal O atoms of the clay contribute to the second hydration shell of the Ca. The planar density of the Ca ion in its global OSSC state (Figure 5 – Ca(C)) suggests that the $Ca^{2+}$ ion sits above the

https://doi.org/10.1346/CCMN.2016.0640310 Published online by Cambridge University Press

hexagonal siloxane cavities of the basal surface of the clay, in agreement with the trends observed for the monovalent ions. Nonetheless, the OSSC for the Ca ion is more localized than the OSSCs for monovalent ions.

Point D in the Ca system refers to the sudden change in gradient of the free-energy curve. This change in gradient is due to the completion of the second hydration shell of the Ca ion as is shown in the water density profile (Figure 3 – Ca(D)). At this point the clay no longer contributes to the hydration shells of the Ca ion, as confirmed by comparing the RDF between Ca and basal clay O atoms with the RDF between Ca and all O atoms (Figure 4 – Ca(D)). The planar density profile for point D (Figure 5 – Ca(D)) shows that the Ca ion preferentially sits above any of the basal O of silicon atoms of the clay. The aforementioned completion of the second coordination shell of the Ca ion is, therefore, achieved with water O atoms.

*Ba-montmorillonite*

The free-energy profile of the montmorillonite-Ba system (Figure 2 – Ba) presents several interesting features not observed in the free-energy profile for Ca. The global energy minimum (point C) corresponds to a clay–ion separation of 4.2 Å with a binding energy of −16.66±1.46 kJ/mol (Figure 2 – Ba(C)). A second, energetically expensive, metastable minimum is also observed in the free-energy curve (point A). This metastable minimum is located at a clay–ion separation value of 1.9 Å and has a binding energy of +18.26±3.55 kJ/mol (Figure 12 – Ba(A)), *i.e.* energy is required to place the ion into this metastable minimum. Two plateaus can also be seen in the free-energy profile of Ba. Point B is at a clay–ion separation of 2.6 Å and has a binding energy of −0.54±1.82 kJ/mol (Figure 2 – Ba(B)), while point D is at a clay–ion separation of 5.8 Å and has a binding energy of −8.38 ± 1.25 kJ/mol (Figure 2 – Ba(D)).

The water-density profiles and RDFs of the Ba-montmorillonite system explain how the ion binds with the mineral surface. At points A and B, the ion is coordinated directly by basal O atoms, forming primary and secondary ISSCs, respectively (Figures 3 and 4 – Ba(A) and Ba(B)). The water structure shows that the global energy minimum occurs when the Ba ion is an OSSC (Figure 3 – Ba(C). In such an occurrence, the basal O atoms of the clay contribute to the second hydration shell of the cation, as can be seen in the corresponding RDF (Figure 4 – Ba(C)). The plateau at point D of the free-energy curve occurs when the second hydration layer of the $Ba^{2+}$ ion begins to completely coordinate with water O atoms (Figure 3 – Ba(D)).

Analysis of the planar density of Ba above the *xy* plane of the clay shows that the two ISSCs are extremely localized above a cavity of the clay siloxane (Figure 5 – Ba(A)) or directly above basal O atoms (Figure 5 – Ba(B)) for the metastable minimum (point A) and plateau (point B), respectively. Similar to all other OSSCs, the OSSC of Ba is localized above one of the hexagonal siloxane cavities of the clay (Figure 5 – Ba(C)), while for all clay–ion separations greater than this distance, the cation freely traverses across the *xy* plane of the clay mineral (Figure 5 – Ba (D)).

## DISCUSSION

The results show that the charge-balancing cations of montmorillonite can form four different stable surface complexes: a primary ISSC located above the siloxane cavity of the basal clay surface; a secondary ISSC located above a basal O atom; an OSSC located loosely above the siloxane cavity; and a SHSSC, which is due to the overlap of the ion's second hydration sphere with the first hydration layer of the clay mineral. No further surface complexes were observed in the simulations.

The formation of two separate ISSCs has been noted in the literature previously. In particular, weakly hydrated interlayer cations ($K^+$, $Cs^+$) have been shown to form ISSCs above the siloxane cavity of the clay interlayer (Park and Sposito, 2002; Nakano *et al*., 2003; Marry and Turq, 2003) while strongly hydrated cations ($Na^+$) form ISSCs on tetrahedral charge sites (Boek *et al*., 1995; Chang *et al*., 1995; Marry and Turq, 2003). The results presented here supplement this previous work, and further suggest that the formation of ISSCs for strongly hydrating cations can occur in the absence of tetrahedral charge-substitutions. The results further imply that the formation of different surface complexes

Table 2. The atomic radius and, therefore, charge to size ratio for each ion. The hydrated radius is calculated as the first minimum in the RDF of each respective ion. The stable surface complex of each ion is linked to the size of the ion's hydration radii and thus charge to size ratio.

| Ion | Atomic radius | Charge/size ratio | Hydrated radius | Stable complex |
|---|---|---|---|---|
| $Na^+$ | 1.90 | 0.53 | 3.23 | OSSC |
| $K^+$ | 2.43 | 0.41 | 3.83 | ISSC |
| $Cs^+$ | 2.98 | 0.34 | 3.87 | ISSC |
| $Ca^{2+}$ | 1.94 | 1.03 | 3.13 | OSSC |
| $Ba^{2+}$ | 2.53 | 0.79 | 3.49 | OSSC |

https://doi.org/10.1346/CCMN.2016.0640310 Published online by Cambridge University Press

is related to the hydration properties of the cation. The stable surface complexation of a cation is related to the hydrated radius of the atom, which are, in turn, inversely proportional to the charge/size ratio of the ion (Table 2).

The weakly hydrated cations, $K^+$ and $Cs^+$, have very similar hydration radius (Table 2), and therefore exhibit similar behavior. In both cases, the primary ISSC is the most energetically favorable state of the ion, and the secondary ISSC and OSSC are metastable. The strongly hydrated monovalent cation, $Na^+$, forms secondary ISSCs, OSSCs, and SHSSCs, and is energetically most stable in its OSSC. Similarly, divalent cations form globally stable OSSCs, in agreement with the relevant literature (Brown and Kevan, 1988; Papelis and Hayes, 1996; Chen and Hayes, 1999; Strawn and Sparks, 1999; Greathouse *et al*., 2000). Barium exhibits an interesting behavior; it is an ion that can form stable primary ISSCs and OSSCs, with plateaus in the free-energy profile associated with the formation of a secondary ISSC and a SHSSC (Zhang *et al*., 2001). This is due to the larger atomic radius of Ba compared with that of Ca, whereby the charge/size ratio of Ba lies somewhere between that of Ca and Ba.

Overall, the results are well converged. The largest errors encountered are for the free-energy profiles of K and Ba. Because the free-energy profile for Ba contains several plateaus and minima, the metadynamic algorithm requires more simulation time to sample all clay−ion separation-phase space compared to other ions. The $K^+$ ion contains a large error due to the lack of convergence in the global energy minimum. This is due to the complex coordination of O atoms to the $K^+$ ion, and is elaborated further below.

### *Accuracy of results*

To further analyze the accuracy of the free-energy profiles, a comparison is made between the equilibrium density profile of the unbiased equilibration simulation with the density profile derived from the free energy. The cation density surrounding the montmorillonite surface is derived from the free energy profile as:

$$\mathrm{n}(d) \propto \exp\left(\frac{-\Delta G(d)}{\mathrm{k_B}T}\right) \quad (5)$$

where $\mathrm{n}(d)$ is the density profile of the ion surrounding the clay, $\Delta G(d)$ is the corresponding free energy at the point $d$, and $\mathrm{k_B}T$ is the thermal energy at temperature $T$. Strictly speaking, because the simulations have been carried out in the NVT ensemble, the calculated free energy is the Helmholtz free energy. Because the simulations had been equilibrated previously in the NPT ensemble, however, one can assume that the Helmholtz and Gibbs free energies are equivalent, under the assumption that the metadynamic bias applied to the ion does not alter the average $z$ spacing of the simulation box.

The analysis shows that the free-energy profiles capture the overall trends observed in the unbiased density profile (Figure 6). In particular, the strongly hydrating cation ($Na^+$, $Ca^{2+}$, and $Ba^{2+}$) density profiles match extremely well. The free-energy profiles generated for $Na^+$, $Ca^{2+}$, and $Ba^{2+}$ capture the essential details of the equilibrium density profile and agree with the previous results of cationic distribution surrounding montmorillonite basal surfaces (Rotenberg *et al.*, 2010; Greathouse *et al.*, 2015). The ion densities calculated from the free-energy profiles for the weakly hydrating cations ($K^+$ and $Cs^+$) vary considerably when compared with the equilibrium density. In the case of K, the metadynamic density underestimates the proportion of secondary ISSCs and OSSCs, suggesting that the free energy calculation overestimates the global binding energy of K to montmorillonite. In contrast, the metadynamic density overestimates the proportion of secondary ISSCs and OSSCs for Cs. This suggests that the free energy profile underestimates the global binding energy of Cs. Clearly, a phenomenon is occurring for the weakly hydrated cations, causing their binding energies to be less accurate than their more strongly hydrated counterparts.

### *Coordination analysis*

The lower accuracy in terms of binding energies for K and Cs can be explained by examining the coordination number of the ion in its most energetically stable state. This is calculated by integrating under the first peak of the radial distribution function (RDF) for each ion (Table 3). Note that, in bulk, the coordination of ions ranges between 6 and 8 O atoms, systematically 1−2 counts over the expected literature values (Varma, 2006). In the SHSSC and OSSC states, the ion remains completely coordinated with water O atoms. In the secondary ISSC, the strongly hydrated $Na^+$ ion is coordinated by five water O atoms and one clay O atom. This, along with the *xy* planar density for Na in its ISSC, proves that the strongly hydrated monovalent cation coordinates directly above a single basal clay O atom. The coordination of the secondary ISSCs for the weakly hydrating cations, $K^+$ and $Cs^+$, shows that 2−3 clay O atoms are contained within the ion's first coordination shell. The secondary ISSCs for K and Cs complex with a triad of basal O atoms, in keeping with previous literature (Park and Sposito, 2002).

Profoundly, for the primary ISSC of K and Cs, the ion is coordinated with six O clay atoms, as well as four/six water O atoms. This drastic change in the total coordination number of K and Cs is the reason that the binding energy calculations are less precise for these ions. The structure of the basal siloxane surface is believed to have formed of ditrigonal cavities (Tesson *et al.*, 2016), rather than the hexagonal cavities observed in these simulations. This suggests a limitation in the force field used within these calculations. The recently

https://doi.org/10.1346/CCMN.2016.0640310 Published online by Cambridge University Press

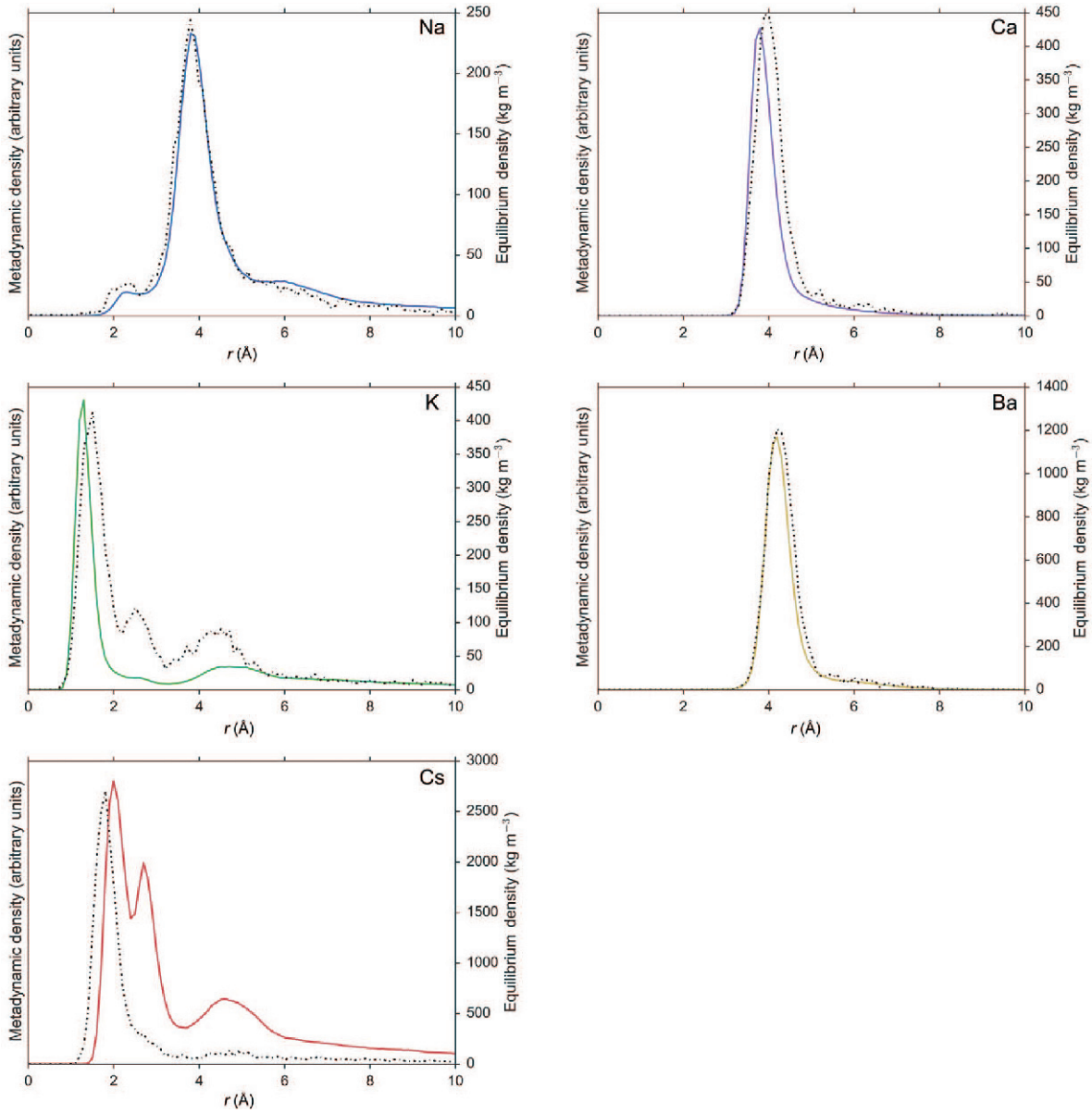


Figure 6. A comparison of ionic densities surrounding the clay surface. The bold line is the density calculated from the free-energy profile, and the dotted line is the density calculated from an unbiased simulation.

developed polarizable force field (Tesson *et al.*, 2016) is parameterized to accurately reproduce the ditrigonal structure of a clay-mineral surface, and may be a more suitable choice going forward, for further binding-energy calculations. The *Interface* force field (Heinz *et al.*, 2013), which includes explicit bonding between surface atoms and dissimilar atom types for basal O atoms, may also be more suited to this task.

### *Equilibrium constants and determining a Hofmeister series for the basal surface of montmorillonite*

To compare binding energies between divalent and monovalent cations at basal surfaces, division of the divalent binding affinity by two (or double the monovalent value) is required because two monovalent ions are required to replace a single divalent ion in identical clay systems. This is valid assuming that the chemical environments of the two monovalent ions do not overly interact with one another. Following this procedure, the results present a Hofmeister-like series for ion adsorption to smectite-mineral surfaces of the form:

$$K^+ > Na^+ > Ca^{2+} > Cs^+ > Ba^{2+}$$

Furthermore, the clay-ion selectivity, *i.e.* the difference in binding-energies between ions $A$ and $B$ ($\Delta\Delta G_A^B$), can be tabulated by considering the difference in global

https://doi.org/10.1346/CCMN.2016.0640310 Published online by Cambridge University Press

Table 3. The coordination number of each ion in each surface complexation state. Expected coordination numbers are taken from Varma (2006).

| Species | Expected CN | Observed CN | Clay CN | Water CN | Clay (%) | Water (%) |
|---|---|---|---|---|---|---|
| Primary ISSC | | | | | | |
| $Na^+$ | 5 | – | – | – | – | – |
| $K^+$ | 6 | 9.3 | 5.9 | 3.4 | 64 | 36 |
| $Cs^+$ | 7 | 11.8 | 5.9 | 5.9 | 50 | 50 |
| $Ca^{2+}$ | 5–7 | – | – | – | – | – |
| $Ba^{2+}$ | 5–7 | 8.5 | 1.1 | 7.4 | 13 | 87 |
| Secondary ISSC | | | | | | |
| $Na^+$ | 5 | 5.9 | 1.1 | 4.8 | 19 | 81 |
| $K^+$ | 6 | 7.6 | 1.9 | 5.7 | 25 | 75 |
| $Cs^+$ | 7 | 9.4 | 2.7 | 6.7 | 29 | 71 |
| $Ca^{2+}$ | 5–7 | – | – | – | – | – |
| $Ba^{2+}$ | 5–7 | 8.5 | 1.1 | 7.4 | 13 | 87 |
| OSSC | | | | | | |
| $Na^+$ | 5 | 5.9 | 0 | 5.9 | 0 | 100 |
| $K^+$ | 6 | 7.6 | 0 | 7.6 | 0 | 100 |
| $Cs^+$ | 7 | 9.3 | 0 | 9.3 | 0 | 100 |
| $Ca^{2+}$ | 5–7 | 8 | 0 | 8 | 0 | 100 |
| $Ba^{2+}$ | 5–7 | 9 | 0 | 9 | 0 | 100 |
| SHSSC | | | | | | |
| $Na^+$ | 5 | 5.8 | 0 | 5.8 | 0 | 100 |
| $K^+$ | 6 | – | – | – | – | – |
| $Cs^+$ | 7 | – | – | – | – | – |
| $Ca^{2+}$ | 5–7 | 8 | 0 | 8 | 0 | 100 |
| $Ba^{2+}$ | 5–7 | 9 | 0 | 9 | 0 | 100 |
| Bulk | | | | | | |
| $Na^+$ | 5 | 5.9 | 0 | 5.9 | 0 | 100 |
| $K^+$ | 6 | 7.8 | 0 | 7.8 | 0 | 100 |
| $Cs^+$ | 7 | 8.2 | 0 | 8.2 | 0 | 100 |
| $Ca^{2+}$ | 5–7 | 8 | 0 | 8 | 0 | 100 |
| $Ba^{2+}$ | 5–7 | 9 | 0 | 9 | 0 | 100 |

binding energies between the respective atoms (Table 4). These values are related to the exchange equilibrium constant ($^{ex}K_A^B$) as (Bourg and Sposito, 2011):

$$\Delta\Delta G = -RT \ln(K) \quad (6)$$

where $^{ex}K_A^B$ relates to the equilibrium reaction between clay, cation $A$, and cation $B$:

$$A - \text{Clay} + B^+ \rightleftharpoons B - \text{Clay} + A^+ \quad (7)$$

The calculated equilibrium constants generally agree with the literature values (Table 5). The selectivity differences are of the order of the thermal energy at 300 K (2.476 kJ) or smaller in all instances. Overall, the values of $K_A^B$ and $\Delta\Delta G_A^B$ show that the basal surface of montmorillonite is weakly selective, with no single ion species preferentially adsorbed to the basal surface of the clay, in agreement with results presented in the literature (Bourg and Sposito, 2011).

Table 4. The clay-ion selectivity ($\Delta\Delta G_A^B$) between ion species.

| | $Na^+$ | $K^+$ | $Cs^+$ | $Ca^{2+}$ | $Ba^{2+}$ |
|---|---|---|---|---|---|
| $Na^+$ | 0.00 | −1.56 | 0.66 | 0.62 | 0.67 |
| $K^+$ | 1.56 | 0.00 | 2.22 | 2.18 | 2.23 |
| $Cs^+$ | −0.66 | −2.22 | 0.00 | −0.04 | 0.01 |
| $Ca^{2+}$ | −0.62 | −2.18 | 0.04 | 0.00 | 0.05 |
| $Ba^{2+}$ | −0.67 | −2.23 | −0.01 | −0.05 | 0.00 |

https://doi.org/10.1346/CCMN.2016.0640310 Published online by Cambridge University Press

Table 5. The exchange equilibrium constants ($^{ex}K_A^B$) for each ion-exchange reaction. Literature values are presented in bold (Bourg and Sposito, 2011; Benson, 1982).

| | $Na^+$ | $K^+$ | $Cs^+$ | $Ca^{2+}$ | $Ba^{2+}$ |
|---|---|---|---|---|---|
| $Na^+$ | – | 1.87 | 0.77 | 0.78 | 0.76 |
| $K^+$ | 0.54<br>**0.58** | – | 0.41 | 0.42 | 0.41 |
| $Cs^+$ | 1.30<br>**1.23** | 2.44 | – | 1.02 | 1.00 |
| $Ca^{2+}$ | 1.28<br>**1.21** | 2.40<br>**1.04** | 0.98<br>**0.26** | – | 0.98 |
| $Ba^{2+}$ | 1.31<br>**1.44** | 2.45 | 1.00 | 1.02 | – |

## CONCLUSIONS

In the present study multiple ensembles of molecular dynamic simulations used in conjunction with well-tempered metadynamics have been used to form the basis for deriving the adsorption energies and mechanisms of simple ions to hydrated mineral surfaces. The methodology is robust and can be transferred to a wide variety of applications to measure the affinity between mineral surfaces and a marked assortment of organic material. The results immediately suggest further ways to improve the accuracy of the calculation of binding energies to clay-mineral surfaces. When calculating the binding energy of poorly hydrating molecules (*e.g.* K and Cs) to clay surfaces, accurate portrayal of the ditrigonal coordination of basal surface O on the siloxane surface is critically important.

Detailed analysis of the water structure and planar *xy* density of cations in their energetically favorable states has revealed four separate surface–ion complexations. Both primary and secondary ISSCs are observed for the weakly and strongly hydrated cations, respectively. A second hydration shell surface complex, whereby the second hydration shell of the cation overlaps with the first hydration layer of the mineral surface, was observed for Na. Outer-shell surface complexes are observed to form for the strongly hydrated ions, $Na^+$, $Ba^{2+}$, and $Ca^{2+}$.

Using the metadynamic algorithm, the results have confirmed the idea of a Hofmeister series for smectite-like minerals. For basal surfaces, the series follows the form:

$$K^+ > Na^+ > Ca^{2+} > Cs^+ > Ba^{2+}$$

and this insight impacts upon a wide range of industrial applications of clay minerals.

Finally, the preference for monovalent ions to be adsorbed to the surface over the naturally occurring divalent ions is important for many industrial applications using the cation-exchange mechanism, whereby an inherently present divalent Ca ion is replaced with a monovalent cation which can improve, for example, water-wettability, and thus increase oil extraction rates in enhanced oil recovery. Future work will involve study of the adsorption of ions as a function of salt concentration, the energetics of intercalated ions as well as calculating the energy barriers at clay-edge sites. Furthermore, the role of tetrahedral substitutions may play a large role in the stability of such ionic systems.

## ACKNOWLEDGMENTS

The authors thank BP for funding Thomas Underwood, the Leverhulme Foundation for funding Valentina Erastova, and the Royal Society for funding H. Chris Greenwell. The work could not have been completed without the use of Durham University's high-performance computing services.

## REFERENCES

Aaqvist, J. (1990) Ion-water interaction potentials derived from free energy perturbation simulations. *The Journal of Phyical Chemistry*, **94**, 8021–8024.

Barducci, A., Bussi, B., and Parrinello M. (2008) Well-tempered metadynamics: A smoothly converging and tunable free energy method. *Physical Review Letters*, **100**, 020603.

Benson, L.V. (1982) A tabulation and evaluation of ion exchange data on smectites. *Environmental Geology*, **4**, 23–29.

Berendsen, H.J.C, Grigera, J.R., and Straatsma, T.P. (1987) The missing term in effective pair potentials. *The Journal of Physical Chemistry*, **91**, 6269–6271.

Bergaya, F., Theng, B., and Lagaly, G., editors (2006) *Handbook of Clay Science.* Elsevier Science, Amsterdam.

Boek, E.S. and Sprik, M. (2003) Ab initio molecular dynamics study of the hydration of a sodium smectite clay. *The Journal of Physical Chemistry B*, **107**, 3251–3256.

Boek, E.S., Coveney, P.V., and Skipper, N.T. (1995) Monte Carlo molecular modeling studies of hydrated Li-, Na-, and K-smectites: Understanding the role of potassium as a clay swelling inhibitor. *The Journal of the American Chemical Society*, **117**, 12608–12617.

Bonomi, M., Branduardi, D., Bussi, G., Camilloni, C., Provasi, D., Raiteri, P., Donadio, D., Marinelli, F., Pietrucci, F., Broglia, R.A., and Parrinello, M. (2009) PLUMED: A portable plugin for free energy calculations with molecular dynamics. *Computer Physics Communications*, **180**, 1961–1972.

https://doi.org/10.1346/CCMN.2016.0640310 Published online by Cambridge University Press

Bourg, I.C. and Sposito, G. (2011) *Ion Exchange Phenomena*; *Handbook of Soil Science*, *Properties and Processes* (2nd edition). CRC Press, Boca Raton, Florida, USA.

Bowers, G.M., Bish, D.L., and Kirkpatrick, R.J. (2008) $H_2O$ and cation structure and dynamics in expandable clays: 2H and 39K NMR investigations of hectorite. *The Journal of Physical Chemistry C*, **112**, 6430–6438.

Brown, D.R. and Kevan, L. (1988) Aqueous coordination and location of exchangeable copper (2+) cations in montmorillonite clay studied by electron spin resonance and electron spin echo modulation. *Journal of the American Chemical Society*, **110**, 2743–2748.

Chang, F.R.C., Skipper, N.T., and Sposito, G. (1995) Computer simulation of interlayer molecular structure in sodium montmorillonite hydrates. *Langmuir*, **11**, 2734–2741.

Chen, C.C. and Hayes, K.F. (1999) X-ray absorption spectroscopy investigation of aqueous Co(II) and Sr (II) sorption at clay–water interfaces. *Geochimica et Cosmochimica Acta*, **63**, 3205–3215.

Coveney, P.V. and Wan, S. (2016) On the calculation of equilibrium thermodynamic properties from molecular dynamics. *Physical Chemistry Chemical Physics*, DOI: 10.1039/C6CP02349E.

Cygan, R.T., Liang, J.J., and Kalinichev, A.G. (2004) Molecular models of hydroxide, oxyhydroxide, and clay phases and the development of a general force field. *The Journal of Phyical Chemistry B*, **108**, 1255–1266.

Downs, R.T. and Hall-Wallace, M. (2003) The American Mineralogist crystal structure database. *American Mineralogist*, **88**, 247–250.

Eisenman, G. (1962) Cation selective glass electrodes and their mode of operation. *Biophysical Journal*, **2**, 259–323.

Gast, R.G. (1969) Standard free energies of exchange for alkali metal cations on Wyoming bentonite. *Soil Science Society of America Journal*, **33**, 37–41.

Gast, R.G. (1972) Alkali metal cation exchange on Chambers montmorillonite. *Soil Science Society of America Journal*, **36**, 14–19.

Greathouse, J.A., Refson, K., and Sposito, G. (2000) Molecular dynamics simulation of water mobility in magnesium–smectite hydrates. *Journal of the American Chemical Society*, **122**, 11459–11464.

Greathouse, J.A., Hart, D.B., Bowers, G.M., Kirkpatrick, R.J., and Cygan, R.T. (2015) Molecular simulation of structure and diffusion at smectite–water interfaces: Using expanded clay interlayers as model nanopores. *The Journal of Physical Chemistry C*, **119**, 17126–17136.

Greenwell, H.C., Jones, W., Coveney, P.V., and Stackhouse, S. (2006) On the application of computer simulation techniques to anionic and cationic clays: A materials chemistry perspective. *Journal of Materials Chemistry*, **16**, 708–723.

Hanshaw, B.B. (1964) Cation-exchange constants for clays from electrochemical measurements. 12th Annual Meeting of the Clay Minerals Society, USA.

Heinz, H., Lin, T.-J., Mishra, R.K., and Emami, F.S. (2013) Thermodynamically consistent force fields for the assembly of inorganic, organic, and biological nanostructures: The INTERFACE force field. *Langmuir*, **29**, 1754–1765.

Hunter, J.D. (2007) Matplotlib: A 2D graphics environment. *Computing in Science and Engineering*, **9**, 90–95.

Koneshan, S., Lynden-Bell, R.M., and Rasaiah, J.C. (1998) Friction coefficients of ions in aqueous solution at 25ºC. *The Journal of the American Chemical Society*, **120**, 12041–12050.

Marry, V. and Turq, P. (2003) Microscopic simulations of interlayer structure and dynamics in bihydrated heteroionic montmorillonites. *The Journal of Physical Chemistry B*, **107**, 1832–1839.

Marry, V., Dubois, E., Malikova, N., Breu, J., and Haussler, W. (2013) Anisotropy of water dynamics in clays: insights from molecular simulations for experimental QENS analysis. *The Journal of Physical Chemistry C*, **117**, 15106–15115

Michaud-Agrawal, N., Denning, E.J., Woolf, T.B., and Beckstein, O. (2011) MDAnalysis: a toolkit for the analysis of molecular dynamics simulations. *Journal of Computational Chemistry*, **32**, 2319–2327.

Nakano, M., Kawamura, K., and Ichikawa, Y. (2003) Local structural information of Cs in smectite hydrates by means of an EXAFS study and molecular dynamics simulations. *Applied Clay Science*, **23**, 15–23.

Ngouana W., B.F. and Kalinichev, A.G. (2014) Structural arrangements of isomorphic substitutions in smectites: Molecular simulation of the swelling properties, interlayer structure, and dynamics of hydrated Cs-montmorillonite revisited with new clay models. *The Journal of Physical Chemistry C*, **118**, 12758–12773.

Papelis, C. and Hayes, K.F. (1996) Distinguishing between interlayer and external sorption sites of clay minerals using X–ray absorption spectroscopy. *Colloids and Surfaces A: Physicochemical and Engineering Aspects*, **107**, 89–96.

Park, S.H. and Sposito, G. (2002) Structure of water adsorbed on a mica surface. *Physical Review Letters*, **89**, 085501.

Pronk, S., Páll, S., Schulz, R., Larsson, P., Bjelkmar, P., Apostolov, R., Shirts, M.R., Smith, J.C., Kasson, P.M., van der Spoel, D., and Hess, B. (2013) GROMACS 4.5: a high-throughput and highly parallel open source molecular simulation toolkit. *Bioinformatics*, **29**, 845–854.

Rotenberg, B., Marry, V., Vuilleumier, R., Malikova, N., Simon, C., and Turq, P. (2007) Water and ions in clays: Unraveling the interlayer/micropore exchange using molecular dynamics. *Geochimica et Cosmochimica Acta*, **71**, 5089–5101.

Rotenberg, B., Morel, J.-P., Marry, V., Turq, P., and Morel-Desrosiers, N. (2009) On the driving force of cation exchange in clays: Insights from combined microcalorimetry experiments and molecular simulation. *Geochimica et Cosmochimica Acta*, **73**, 4034–4044.

Rotenberg, B., Marry, V., Malikova, N., and Turq, P. (2010) Molecular simulation of aqueous solutions at clay surfaces. *Journal of Physics: Condensed Matter*, **22**, 284114.

Shroll, R.M. and Smith, D.E. (1999) Molecular dynamics simulations in the grand canonical ensemble: Application to clay mineral swelling. *The Journal of Chemical Physics*, **111**, 9025–9033.

Smith, D.E. and Dang, L.X. (1994a) Computer simulations of cesium-water clusters: Do ion-water clusters form gas-phase clathrates? *The Journal of Chemical Physics*, **101**, 7873.

Smith, D.E. and Dang, L.X. (1994b) Computer simulations of NaCl association in polarizable water. *The Journal of Chemical Physics*, **100**, 3757.

Strawn, D.G. and Sparks, D.L. (1999) The use of XAFS to distinguish between inner-and outer-sphere lead adsorption complexes on montmorillonite. *Journal of Colloid and Interface Science*, **216**, 257–269.

Suter, J.L., Anderson, R.L., Greenwell, H.C., and Coveney, P.V. (2009) Recent advances in large-scale atomistic and coarse-grained molecular dynamics simulation of clay minerals. *Journal of Materials Chemistry* , **19**, 2482–2493.

Swenson, J., Bergman, R., and Howells, W.S. (2000) Quasielastic neutron scattering of two-dimensional water in a vermiculite clay. *The Journal of Chemical Physics*, **113**, 2873–2879.

Teppen, B.J. and Miller, D.M. (2006) Hydration energy determines isovalent cation exchange selectivity by clay minerals. *Soil Science Society of America Journal*, **70**, 31-40.

Tesson, S., Salanne, M., Rotenberg, B., Tazi, S., and Marry, V.

(2016) Classical polarizable force field for clays: Pyrophyllite and talc. *The Journal of Physical Chemistry C*, **120**, 3749–3758.

Tribello, G.A., Bonomi, M., Branduardi, D., Camilloni, C., and Bussi, G. (2014) PLUMED 2: New feathers for an old bird. *Computer Physics Communications*, **185**, 604–613.

Underwood, T., Erastova, V., Cubillas, P., and Greenwell, H.C. (2015) Molecular dynamic simulations of montmorillonite–organic interactions under varying salinity: An insight into enhanced oil recovery. *The Journal of Physical Chemistry C*, **119**, 7282–7294.

Viani, A., Gualtieri, A.F., and Artioli, G. (2002) The nature of disorder in montmorillonite by simulation of X-ray powder patterns. *American Mineralogist*, **87**, 966–975.

William Humphrey, A.D. (1996) VMD: visual molecular dynamics. *Journal of Molecular Graphics*, **14**, 33–38.

Zhang, P.C., Brady, P.V., Arthur, S.E., Zhou, W.Q., Sawyer, D., and Hesterberg, D.A. (2001) Adsorption of barium (II) on montmorillonite: an EXAFS study. *Colloids and Surfaces A: Physicochemical and Engineering Aspects*, **190**, 239–249.

Zhang, Y. and Cremer, P.S. (2006) Interactions between macromolecules and ions: the Hofmeister series. *Current Opinion in Chemical Biology*, **10**, 658–663.

(*Received 12 October 2015; revised 29 September 2016; Ms. 1049; AE: Xiandong Liu*)